



## Full length article



## The origin of deformation induced topological anisotropy in silica glass

Sudheer Ganiseti<sup>a,b,c</sup>, Achraf Atila<sup>a,d,e</sup>, Julien Guérolé<sup>b</sup>, Aruna Prakash<sup>f</sup>, Jürgen Horbach<sup>g</sup>,  
Lothar Wondraczek<sup>h</sup>, Erik Bitzek<sup>a,d,\*</sup>

<sup>a</sup> Department of Materials Science and Engineering, Institute I, Friedrich-Alexander-Universität Erlangen-Nürnberg (FAU), Erlangen, 91058, Germany

<sup>b</sup> Université de Lorraine, CNRS, Arts et Métiers, LEM3, Metz, 57070, France

<sup>c</sup> Department of Chemistry and Bioscience, Aalborg University, Aalborg, 9220, Denmark

<sup>d</sup> Computational Materials Design, Max-Planck-Institut für Eisenforschung, Düsseldorf, 40237, Germany

<sup>e</sup> Department of Material Science and Engineering, Saarland University, Saarbrücken, 66123, Germany

<sup>f</sup> Micro-Mechanics & Multiscale Materials Modeling (M<sup>2</sup>), Institute of Mechanics and Fluid Dynamics, Technische Universität Bergakademie Freiberg (TUBAF), Freiberg, 09599, Germany

<sup>g</sup> Institut für Theoretische Physik II, Heinrich-Heine-Universität Düsseldorf, Düsseldorf, 40225, Germany

<sup>h</sup> Otto Schott Institute of Materials Research, Friedrich Schiller University Jena, Jena, 07743, Germany

## ARTICLE INFO

## Keywords:

Silica glass

Plasticity

Molecular dynamics

Stereographic projection

## ABSTRACT

Oxide glasses with a network structure are omnipresent in daily life. Often, they are regarded as isotropic materials; however, structural anisotropy can be induced through processing in mechanical fields and leads to unique materials properties. Unfortunately, due to the lack of local, atomic-scale analysis methods, the microscopic mechanisms leading to anisotropy remained elusive. Using novel analysis methods on glasses generated by molecular dynamics simulations, this paper provides a microscopic understanding of topological anisotropy in silica (SiO<sub>2</sub>) glass under mechanical loads. The anisotropy observed in silica glass originates from a preferred orientation of SiO<sub>4</sub> tetrahedra at both short- and medium-range levels that can be controlled via the mode of mechanical loading. The findings elucidate the relation between the deformation protocol and the resulting anisotropic structure of the silica network (involving both persistent and transient effects), and thus provide important insight for the design of oxide glasses with tailored materials properties.

## 1. Introduction

Throughout the centuries, oxide glasses have attracted the interest of scientists and engineers due to the sheer number of possible compositions, allowing the development of new glasses that address societal and technological needs [1]. Current areas of glass design include flexible screens for mobile devices, optical fibers with super low signal loss, and mechanically resistant solar modules [2,3]. Many of these applications result from empirical studies, which have now arrived at a crossroad: for the targeted design of new glasses and to extend further the range of their applications, a fundamental understanding of the relationship between glass composition, processing, structure, and properties is required. Structurally, oxide glasses consist of glass-forming cations surrounded by oxygen polyhedra. These polyhedra share corners, establishing a three-dimensional random network. The paradigm of a network glass is silica, in which corner-shared SiO<sub>4</sub> tetrahedra [4] form Si-O rings of different sizes [5]. Due to this amorphous structure, oxide glasses such as silica are typically regarded as being isotropic. However, glasses can exhibit anisotropic properties when processed accordingly.

This is demonstrated most prominently by optical birefringence, which is used to visualize residual or transient mechanical stress embedded in a glass object, for example, monitoring stress fields in Prince Rupert's drops [6]. As another example, homogeneous anisotropy can be induced in glasses by fiber drawing [7–10]. Such anisotropy, caused by deformation of the viscous melt [11,12], is only reversible by thermal annealing. Therefore, in the following, it is referred to as *persistent* anisotropy. In contrast, glasses can also show elastic or *transient* anisotropy, which is present only during mechanical loading, e.g., as observed in stress-induced reversible birefringence [13]. Mechanical loading can, of course, also lead to persistent anisotropy that remains after switching off the load and is then reflected, e.g., in the occurrence of residual stresses [14].

Transient anisotropy is of fundamental importance during the deformation and fracture of oxide glasses; it constitutes the initial response of the glass network to mechanical load and thereby defines all subsequent mechanical reactions. The specific directional preference of molecular-scale deformation routes is a direct result of the

\* Corresponding author at: Computational Materials Design, Max-Planck-Institut für Eisenforschung, Düsseldorf, 40237, Germany.

E-mail address: [e.bitzek@mpie.de](mailto:e.bitzek@mpie.de) (E. Bitzek).

combination of highly directional bonding among the network-forming species, structural disorder, the resulting occurrence of heterogeneous rigidity [15,16], and (if present) further interatomic interactions with reduced directionality (e.g., ionic interactions from cation constituents with lower bond covalency, the so-called network modifiers). However, the specific nature, molecular mechanism, and similarities to persistent anisotropy (which can be studied ex-situ) have been elusive, in particular, for the archetypal case of vitreous silica. Silica is the backbone of practically all contemporary glass materials which exist for widespread application. From a viewpoint of mechanical response, the other chemical components which make up a real-world glass are either highly mobile (such as the network modifiers with predominantly ionic bonding and/or high ion polarizability) or embedded as part of the backbone network (such as secondary network forming species, e.g.,  $B_2O_3$  or  $Al_2O_3$ ) [17]. Therefore, understanding the transient anisotropy of the silica backbone appears to hold a key towards designing glasses with adapted mechanical performance.

Persistent anisotropy can be caused by inhomogeneities in the glass that are either becoming aligned or deformed through the deformation process; this effect was denoted *shape anisotropy* [18]. Persistent anisotropy has, however, also been observed in the absence of inhomogeneities. Early observations of optical anisotropy were explained by frozen-in elastic deformation, assuming that the glass structure consists of elastic and fluid units [19]. Takamori and Tomozawa [20] provided the first systematic review on anomalous birefringence occurring in a range of oxide glasses, which they related to frozen-in strain and microstructural orientation. The structural origin of mechanically-induced anisotropy in metallic glasses subjected to uniaxial tensile stress during creep was studied using X-ray diffraction by Suzuki et al. [21]. From their observations, they conjectured a model of bond orientation anisotropy, in which atoms in the unloaded glass have more nearest neighbor atoms in the direction perpendicular than parallel to the tensile axis [21].

In contrast to metallic glasses, anisotropy in silica glass was shown to be related to the changes at the medium-range structure [12,22]. Studies on uniaxially compressed silica glass at room temperature (RT) that was unloaded showed a remaining strain [12]. This was characterized from the deviation of the first sharp peak from a perfectly radial diffractogram, and it was suggested that the anisotropy was caused by directionality in permanent densification through changes in the medium-range structure [12]. Similar conclusions were also drawn from Brillouin scattering experiments on uniaxially compressed silica glass [22]. In situ mechanical quenching experiments on nanoscale silica spheres were recently performed in a transmission electron microscope [23]. Changes in the Young's modulus after the spheres were uniaxially compressed under the electron-beam were attributed to the reorientation of the Si–O–Si bonds away from the compression axis, leading to an anisotropic structure [23].

In contrast to experiments, atomistic simulations allow for a direct, local analysis of the glass structure [24]. Molecular dynamics (MD) simulations showed that mechanical loading could induce structural anisotropy [11,25,26]. In particular, a change of the medium-range structure was demonstrated using the fabric tensor to characterize the mean orientation of the Si–O–Si bonds. It was shown that silica glass plastically deformed under shear can exhibit structural anisotropy even in the unloaded state [11]. An MD study that tried to mimic the drawing process of silica fibers at high temperatures using uniaxial tensile tests in a fully periodic system showed that the normals of small rings tend to orient parallel to the stress axis during the drawing and cooling processes [26]. In contrast, the 6-membered rings have their surface normals oriented orthogonal to the loading axis [26]. These preferential orientations persist when cooled to room temperature (under load), leading to an anisotropic glass structure and anisotropic elastic properties [26]. For a silica glass subjected to compression at 1000 K, it was observed that the three-membered rings have their plane normal orthogonal to the compression axis [25].

While MD simulations have provided some insights into the experimental findings, the use of different flow regimes and/or loading modes has hindered a one-to-one comparison between MD studies and experiments, which led to the lack of clear conclusions on the origins of the structural anisotropy observed in silica glass. In particular, it is not clear whether mechanically induced persistent anisotropy implies similar structural changes than transient anisotropy and whether persistent anisotropy caused by deformation at room temperature is comparable to anisotropy produced around or above the glass transition temperature ( $T_g$ ), e.g., during wire drawing.

Here we show that transient and persistent anisotropy induced by uniaxial deformations at RT have clearly different structural origins. Using stereographic projections, we demonstrate that during uniaxial tension and compression, the  $SiO_4$  tetrahedra and the Si–O rings reorient with respect to the loading axis, leading to transient anisotropy. Persistent anisotropy in the unloaded glass is caused by permanent changes in bond topology and is more pronounced after compression than after tension due to the larger plastic strains reached in the former. In addition, we demonstrate that persistent anisotropy induced through loading at temperatures around  $T_g$  is structurally different from anisotropy produced by RT deformation.

## 2. Materials and methods

### 2.1. Glass preparation

The atomic interactions were modeled by the first principles based polarizable force field developed by Kermode et al. [27]. Additional simulations using the BKS potential [28,29] showed no qualitative differences; see supplementary material Fig. S1. The initial, pristine glass sample was prepared by deforming and rescaling an  $\alpha$ -quartz structure containing 72000 atoms into a cubic simulation box to match with the experimental density of  $2.2 \text{ g cm}^{-3}$  of silica glass [30]. Periodic boundary conditions (PBC) were used along all directions. This sample was molten at 5000 K in the NVE ensemble for 10 ps, kept at this temperature for 10 ps in the NVT ensemble, and 100 ps in the NPT ensemble at 0 MPa while maintaining a cubic simulation box. The sample was cooled to 300 K in the NPT ensemble at a cooling rate of  $10^{13} \text{ K s}^{-1}$  and 0 MPa, resulting in a glass with a density of  $2.39 \text{ g cm}^{-3}$ , see also Tab. S1 in the supplementary material. For this quenching rate, the glass transition temperature was determined to  $T_g = 3000 \text{ K}$ . Additional glasses were prepared with cooling rates of  $2 \times 10^{13} \text{ K s}^{-1}$  and  $1 \times 10^{14} \text{ K s}^{-1}$ . Nosé–Hoover thermo- and barostats were used to perform the constant temperature and pressure simulations [31,32]. A timestep of 0.1 fs was used for the MD simulations at temperatures above 1000 K and 1 fs for temperatures below.

### 2.2. Deformation

The equilibrated stress-free isotropic glass sample ('pristine sample') was subjected to uniaxial deformation by tension or compression at 300 K. The deformation was applied by homogeneously scaling the samples along the  $x$ -direction at a strain rate of  $5 \times 10^8 \text{ s}^{-1}$ , while maintaining zero stress in the orthogonal directions. Additional deformations were performed with strain rates of  $1 \times 10^9 \text{ s}^{-1}$  and  $5 \times 10^9 \text{ s}^{-1}$ , see supplementary material Fig. S2. At strains of  $\epsilon_x$  (where  $x = 2\%, 5\%, 7\%$  and  $17\%$ , during tension and  $x = 2\%, 5\%, 7\%, 17\%, 20\%, 25\%, 30\%, 35\%$  and  $40\%$ , during compression) the sample was unloaded back to the stress-free state. Additional simulations to investigate the effect of the cooling rate and deformation temperature on the stress–strain response and anisotropy index are shown in Fig. S3 and Fig. S4 in supplementary materials.

Deformations at higher temperature to mimic the wire-drawing process were performed at  $T_g$ . Here, the melt was first cooled under temperature and pressure control from 5000 K to 3000 K with a cooling rate of  $10^{13} \text{ K s}^{-1}$  while keeping zero stress in all axes. The stress-free

sample at 3000 K was subjected to uni-axial tension or compression up to 17% strain along the  $x$ -axis while keeping zero stress on the other two orthogonal axes. After the deformation, the samples were quenched to 300 K while allowing the box and atoms to relax the accumulated stress using a cooling rate of  $10^{14}$  K s $^{-1}$ . The resulting glasses have densities of 2.35 g cm $^{-3}$  for the glasses pre-deformed in tension and 2.43 g cm $^{-3}$  for the one pre-deformed in compression at  $T_g$ .

### 2.3. Anisotropy index

The change of the orientation of a pair of atoms during the loading and unloading is monitored and quantified by the anisotropy index ( $\alpha$ ). The anisotropy index is a scalar value obtained by calculating the eigenvalues ( $\lambda_i$ ) of the fabric tensor  $F = \langle n \otimes n \rangle$  [11] as given in Eq. (1), and is normalized in a way that it will vary between 0 and 1,

$$\alpha = \sqrt{\frac{3}{2} \sum_{i=1}^3 \left( \lambda_i - \frac{1}{3} \right)^2} \quad (1)$$

For an isotropic material,  $\alpha = 0$ , and in the case of full anisotropy  $\alpha = 1$ , higher values mean higher anisotropy in the medium. We computed  $\alpha$  for Si–O, Si–Si, and O–O pairs, and it is referred to as  $\alpha(\text{Si–O})$ ,  $\alpha(\text{Si–Si})$ , and  $\alpha(\text{O–O})$ , respectively.

### 2.4. Anisotropic radial distribution function

To capture the short-range order's directionality, a suitable expansion of the RDF onto spherical harmonics must be utilized. Particularly, we take the following expansion into spherical harmonics  $Y_{lm}(\theta, \phi)$

$$g(r) = \sum_{l=0}^{\infty} \sum_{m=-l}^l g_{lm}(r) Y_{lm}(\theta, \phi) \quad (2)$$

where  $l$  and  $m$  are the degree and order of the spherical harmonic and  $g_{lm}$  is the expansion coefficient. During a uniaxial deformation, the deformation axis will be the symmetry axis. Checking the spherical harmonic functions,  $Y_{20}$  best captured this behavior. The expansion coefficients of the RDF into the  $Y_{20}$  spherical harmonic is given as,

$$g_{20}^{\alpha\beta} = \frac{\sqrt{15}V}{\sqrt{16\pi}N_{\alpha}N_{\beta}} \left\langle \sum_i^{N_{\alpha}} \sum_{j \neq i}^{N_{\beta}} \delta(|r_i^{\alpha} - r_j^{\beta}| - r) \frac{2(z_i^{\alpha} - z_j^{\beta})^2 - ((x_i^{\alpha} - x_j^{\beta})^2 + (y_i^{\alpha} - y_j^{\beta})^2)}{(r_i^{\alpha} - r_j^{\beta})^4} \right\rangle, \quad (3)$$

where  $\alpha$  and  $\beta$  are the atom types,  $N_{\alpha}$  and  $N_{\beta}$  are their corresponding number of atoms,  $V$  is the volume of the simulation box,  $x$ ,  $y$ , and  $z$  are the atomic position in Cartesian coordinates. This function is positive when more bonds between atom types  $\alpha$  and  $\beta$  of length  $\langle |r_i - r_j| \rangle$  are oriented in parallel to the loading axis than orthogonal to it, and negative when there are more bonds of a certain length orthogonal than parallel to the loading axis.

### 2.5. Stereographic projections of tetrahedra face normals and rings

To the best of our knowledge, the stereographic projection is used for the first time to characterize the structure of oxide glasses in this work. The steps that we used to adapt this method to our needs are detailed in the supplementary materials. First, the tetrahedral face normal calculation was made by finding the nearest neighbors of each Si atom. Then, the four-fold coordinated Si atoms were identified, each Si atom and its four nearest neighboring O atoms were separated, these five atoms together were referred to as tetrahedron, each tetrahedron has four faces, and each face has three atoms. Next, the normal vector of each face of the tetrahedra was computed using the position vectors of the three O atoms. Lastly, these vectors were normalized and then stereographically projected on the required plane as described by the procedure detailed in the supplementary materials.

For the ring normals, a similar approach was used where all rings of a given sample were identified using the RINGS code [33]. Each ring's Si and O atoms were separated; see Fig. S5(d) for an example with a six-membered ring. The center of mass of each ring was computed based on the position of the atoms, see Fig. S5(e). Then, each ring was discretized into triangles with 2 neighboring Si atoms and the center of mass of the corresponding ring. After that, the normal vector of each triangle was computed, see Fig. S5(f). The ring normal is determined as the normalized average of all its triangle normals, see Fig. S5(g). Lastly, all the normals of the same-sized rings were projected on the required plane using stereographic projection by following the procedure above (see Fig. S5(h–j)).

### 2.6. Bond statistics

Bond statistics following [34] was used to determine the number of atoms with new, switched, or broken bonds. This was achieved by comparing the deformed configuration with the pristine glass configuration and finding the differences in bonding topology between them. Each atom has a unique ID. This allows to determine atoms with broken or added bonds by comparing the number of their nearest neighbors with respect to the reference configuration. Atoms with switched bonds have the same number of nearest neighbors as in the reference configuration but have at least one nearest neighbor with a different ID than in the reference configuration.

## 3. Results and discussions

### 3.1. Deformation of silica glass and characterization of structural anisotropy

The usual structural characterization of the simulated silica glass at RT are shown in the supplementary material, Fig. S6, and these are consistent with the data reported in the literature from both experiments [5] and simulations [27]. The stress–strain curves of pristine silica glass subjected to tension and compression at RT are shown in Fig. 1 and show brittle fracture in the case of tension and plastic flow in compression. Unloading simulations to zero stress were performed starting from different values of the maximum strain as depicted in Fig. 1(a and b). Unloading from strains beyond 12% tensile strain resulted in a permanent plastic strain. For compressed samples, a permanent plastic strain was observed for unloading from strains beyond 10%. The densities after unloading from different loads are provided in the supplementary material, Tab. S1.

During straining, the radial distribution function and the bond angle distribution are clearly changed from their pristine state, see Fig. S6 in the supplementary material. However, after unloading, only negligible differences are observed, and these isotropic measures cannot be used to characterize anisotropy. Therefore, following earlier studies [11], the anisotropy was first quantified by the anisotropy index  $\alpha$  (see method section for details), which is shown in Fig. S7 in the supplementary material. The increase of  $\alpha(\text{Si–Si})$  and  $\alpha(\text{Si–O})$  during the loading up to the yield stress shows that the deformation induces some alignment in the Si–Si and Si–O bonds. This transient anisotropy during loading was present irrespective of the deformation mode. Significant persistent anisotropy was only observed in compression, as shown in Fig. S7(d). Simulations performed at different strain rates and on samples produced with different cooling rates showed that the observed trends regarding transient and persistent anisotropy do not depend on those parameters. However, the degree of anisotropy and the remaining plastic strain depends on the cooling and strain rates; see Figures S3 and S2 in the supplementary material. Deformation at higher temperatures showed that anisotropy is affected by the deformation temperature (see supplementary material Fig. S4).

To characterize in detail preferred orientations in short-range order, we use the spherical harmonic expansion of the pair distribution function [35]. In the case of an axial symmetry, such as in the current

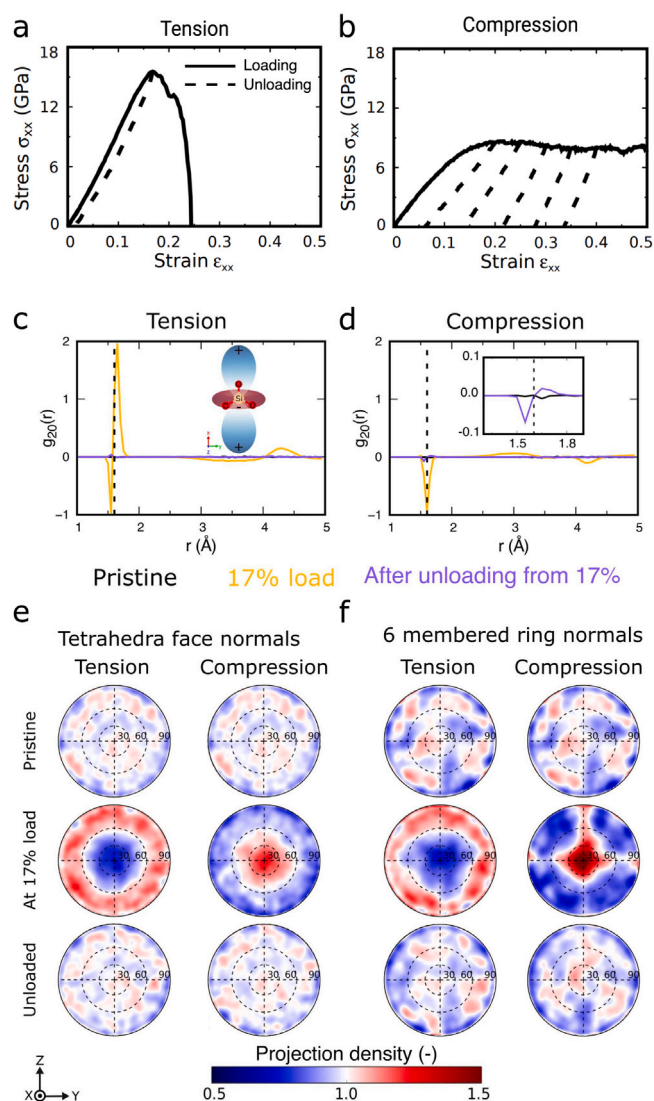


**Fig. 1.** Top row: Stress–strain response in tension (a) and compression (b) ( $\dot{\epsilon} = 5 \times 10^8 \text{ s}^{-1}$ ,  $T = 300 \text{ K}$ ). Middle row: Projection of the Si–O pair distribution function onto the spherical harmonic  $Y_{20}$  for glasses at different stages of deformations in tension (c) and compression (d). Solid black, yellow, and purple lines indicate the samples at initially 0% strain, loaded to 17% strain, and stress-free, unloaded from 17% strain. The dashed lines indicate the position of the average Si–O bond length in the pristine sample. If there are more bonds of the same length  $r$  in the loading ( $x$ ) direction than in the orthogonal directions,  $g_{20}(r)$  is positive and vice-versa for negative  $g_{20}(r)$ . Bottom row: Stereographic projection maps of the tetrahedra face normals (e) and 6-membered rings normals (f) at different stages of deformation. The color indicates the density in the normalized projection map, see Fig. S5 in the supplementary material for the definition of stereographic projections. (For interpretation of the references to color in this figure legend, the reader is referred to the web version of this article.)

study, the radial distribution function is projected on the spherical harmonic  $Y_{20}$ ; see the methods section for more detail. Fig. 1(c and d) shows the spherical harmonic coefficient  $g_{20}(r)$ , which describes the intensity of spherical harmonic term  $Y_{20}$  for the pristine glass, loaded to 17% in tension and compression and unloaded from 17% strain to zero stress. In the following, we will focus on these samples; loading up to and unloading from higher strains resulted in qualitatively similar behavior. For the pristine glass,  $g_{20}(r)$  shows that the Si–O bonds are distributed randomly without preferential orientation and indicates that pristine silica glass has an isotropic short-range structure. During tension, Fig. 1(c), more Si–O bonds that are longer than the average bond length in a pristine sample ( $\langle l_{\text{Si-O}} \rangle = 1.6 \text{ \AA}$  see supplementary information, Fig. S6) are aligned in the loading

direction than in directions orthogonal to it, while shorter bonds tend to be oriented orthogonal to the loading axis. The isotropic structure is mostly recovered when unloaded back to the zero-stress state, as indicated by the absence of noticeable peaks after the unloading. In contrast, the behavior during compression is different from the one in tension, and only one negative peak centered around  $\langle l_{\text{Si-O}} \rangle$  is observed, indicating that there are more Si–O bonds of average length oriented perpendicular to the loading axis than parallel to it. Interestingly, the unloaded sample after compression shows qualitatively the same  $g_{20}(r)$  signature as the glass loaded during tension: shorter than average bonds oriented mostly orthogonal to the loading axis, and more elongated bonds along the loading axis (Fig. 1(d)).

The glass structure can be further characterized by determining the orientation of tetrahedra face normals, see the methods section and the supplementary material for more details on the method. Fig. 1(e) shows the normalized stereographic projections of tetrahedra face normals on the  $yz$ -plane in both tension and compression for the pristine, loaded, and unloaded samples. As shown for the pristine silica glass, the normalized stereographic projection of tetrahedra face normals shows that the tetrahedra are randomly oriented in all possible directions without having any preferential orientation. In the loaded sample in tension, the normalized stereographic projections indicate that most tetrahedra faces are oriented perpendicular to the tensile axis. At the same level of strain in compression, the normalized stereographic projection shows that most of the tetrahedra faces are oriented perpendicular to the compression axis. In the unloaded samples, the normalized stereographic projections show a uniform orientation of the tetrahedra.

The ring statistic presented in Fig. S6 shows that the number of 6-membered rings, which represent the majority of the rings in our glass, is only slightly affected by the deformation. Fig. 1(f) shows the normalized stereographic projection of 6-membered ring normals for the pristine silica, loaded, and unloaded samples (see the methods section and supplementary materials Fig. S5 for the computation of ring normals). Although a uniform orientation of ring normals is expected in pristine silica, insufficient averaging due to the small sample leads to small deviations of the projected 6-membered ring normals from a uniform density, see Fig. 1(f). However, a clear orientation of the 6-membered ring plane normals away from the loading axis is visible for the sample loaded in tension. Under compression, the loaded samples show a strong preferential orientation of 6-membered ring-plane normals along the compression axis. After unloading to zero stress, a uniform orientation of 6-membered ring normals is observed for both tension and compression.

### 3.2. Evolution of bond topology under load

Fig. 2(a), shows the evolution of new, switched, and broken bonds during tensile loading to 17% strain and unloading from it. The methodology of computing the bond statistics follows Ref. [34] and is described in the method section. The percentage of atoms which switched neighbors before yielding at around 12% tensile strain is less than 0.5%. With yielding, this fraction increases to 1.5% at 17% strain. During unloading, some more bond switching occurs, and then the percentage of atoms with switched bonds stays roughly constant, indicating that the new bonding topology is maintained with unloading. As expected for tensile loading, the percentage of atoms with broken bonds increases, but less strongly than the number of switched bonds, and only a negligible number of atoms adds bonds. While the number of newly formed bonds stays constant, some broken bonds are healed during unloading. During compression, Fig. 2(b), only very few bonds are broken, and more bonds are formed than switched until yield when the percentage of bond switching significantly increases from about 10% strain on. However, even in compression, the percentage of atoms with changed bonding topology remain below 3% at 17% strain. After unloading from 17% strain to zero stress, the percentage of atoms with broken bonds decreases slightly, and the percentage of atoms with new bonds reduces from 0.9% to 0.3%, while the number of switched bonds further increases during the initial stages of unloading and then only slightly decreases.

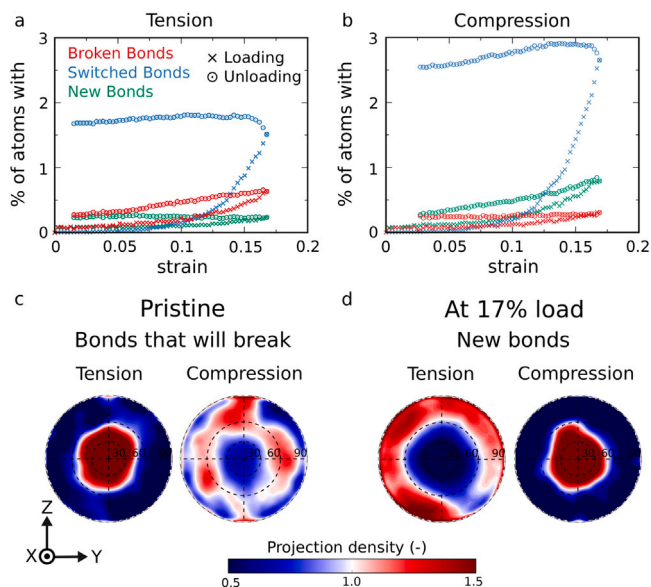


Fig. 2. Top: Evolution of broken (red), switched (blue), and new (green) bonds during tension (a) and compression (b). Solid lines correspond to loading to 17% strain, and dashed lines mark the unloading from 17% strain. Bottom: Stereographic projections for tension and compression showing the orientation of bonds that will be broken during the straining to 17% (c) and for bond that formed during the straining to 17% (d). The orientation of the bonds that will be broken is shown in the pristine glass, while that of the newly formed bonds is shown in the loaded samples.

### 3.3. Origin of transient and persistent anisotropy

The orientation of the bonds that will be broken at 17% strain and the bonds that will be newly formed at 17% strain are shown in Fig. 2(c and d). Although in tension only relatively few bonds are broken before reaching the maximal tensile stress, the bonds that break were already in the pristine sample clearly oriented parallel to the loading axis. In compression, the very few bonds that break were preferably oriented at about  $60^\circ$  to the compression axis before deformation. Most of the bonds that were newly formed during tension make at 17% strain an angle between  $60$  and  $90^\circ$  with the tensile axis. The new bonds formed during compression make at 17% compression preferentially an angle between  $0$  and  $30^\circ$  with the compression axis.

In the elastic regime in compression, the strain is accumulated by reducing Si–O bond lengths in the direction of compression and/or by changing Si–O–Si angles, leading to transient anisotropy. The major portion of densification in this regime is associated with rearranged network topology upon reduced Si–O–Si bond angles, which is in consistent with Trease et al. [36]. The reduced Si–O bond length is in consistent with Benmore et al. [37]. When the sample is unloaded from this regime, the stored elastic strain is released, and the silica glass returns to its initial state of isotropy. Unloading from the plastic regime resulted in a finite plastic strain at zero stress, and the unloaded glass showed structural anisotropy. The transition from elastic to plastic regime is correlated with a strong increase in the number of atoms with switched bonds.

Persistent anisotropy can thus be understood in terms of changes in bond topology through plastic deformation and bond switching, as opposed to simple ring deformation reactions. As shown in Fig. 2(c and d), this bond switching is not random. Due to the Poisson expansion orthogonal to the compressive axis, bonds in this direction are elongated and, therefore, more prone to bond switching or breaking. New bonds are then preferentially formed along the compression axis, where atoms are brought closer together. Upon unloading, the new bonding topology is maintained (only few bond switching events during unloading, Fig. 2(b)). However, the newly formed bonds along the

loading axis become now elongated as the atoms move further away. The initial bonding partner, however, can just relax, leading to shorter bonds orthogonal to the loading axis. This explains the  $g_{20}(r)$  signature of the persistent anisotropy introduced by pre-compression, Fig. 1(d). The same rationale applies to glasses pre-deformed in tension, however, there the significantly reduced tendency for bond-switching compared to compression leads to only weak anisotropy.

Compression of silica glass is well known to result in densification through (1) decreasing the Si–O–Si bond angles, (2) by enlarging the Si–O bond lengths, and (3) by increasing the number of over-coordinated Si [36,37]. It is, however, important to note that (a) densification is usually observed as persistent densification, i.e., after load removal; and that (b) densification is commonly examined after samples were subjected to hydrostatic strain states or similar cases, in which the flow of material is restricted to a certain volume like in the case of indentation. Our observations show that under purely uniaxial compression, i.e. by allowing Poisson expansion, the densification is much less than under comparable hydrostatic strains, see Table S1 in supplementary material. The densification in our simulations of uniaxial compression is due to the reduction of Si–O–Si bond angles, see Fig. S6d in the supplementary material and not by bond shortening (Fig. S6b) or by overcoordinated Si atoms (Fig. S8). Changes in bonding topology, bond lengths and bond angles after compression, can, however, due to different boundary conditions, very well be different for uniaxially compressed and indented silica glass. This is important when comparing our results to complementary work, e.g., by He et al. [38,39]. Furthermore, scalar measures like bond-length distributions cannot provide significant information on densification by uniaxial compression, as changes in different directions can cancel each other out. Finally, the notion of persistent densification implies also the possibility of transient densification which, as our work on anisotropy has shown, might have different topological signatures compared to persistent densification.

While the deformation-induced anisotropy was studied here only for silica glass, the results can be used to discuss what can happen when modifiers (e.g.  $\text{Na}_2\text{O}$ ) are present in the glassy matrix. Silica glass has a high structural homogeneity, which renders it difficult to induce structural anisotropy. A higher level of structural anisotropy is expected in glasses that contain structural inhomogeneities due to the presence of highly directional covalent bonds, i.e., Si–O and modifiers–O bonds with less to no bond directionality. The presence of modifiers within the glass leads to depolymerization of the structure by transforming the bridging oxygens (BO) to non-bridging oxygen (NBO). For example, meta-silicate and meta-phosphate glasses have a chain-like structure made of glass former tetrahedra that are linked by BOs. These chains are separated by modifier–NBO bonds, which have low bond strength compared to Si–BO or P–BO bonds. Breaking these chains under load can be harder than breaking the bonds associated with the non-bridging oxygen. As reported by Yang et al. [9] and Endo et al. [8], a higher level of anisotropy can be induced by freezing these chains into a preferential orientation.

### 3.4. Direct observation of mechanisms leading to anisotropy

The mechanisms and structural changes causing anisotropy can not only be inferred from analysis averaging over the entire sample, Figs. 1 and 2, but can also be directly observed in the simulations. Fig. 3 and movie M1 show the process in detail, where during compression to 17% strain, the central Si atom of the shown tetrahedron switches a bond to a nearby O atom. This leads to a bond loss in the orthogonal direction to the compression axis and a new bond along the loading axis. During unloading, the newly formed bond does not switch back to the original configuration, but the tetrahedron rotates to adjust for the increase in sample length during unloading. The middle and lower row of Fig. 3 show in addition the change of orientation of the ring and tetrahedra normals as well as the relative bond length of differently oriented Si–O bonds of the tetrahedron. This provides direct evidence for our interpretation of Figs. 1(d–e) and 2(c, d).

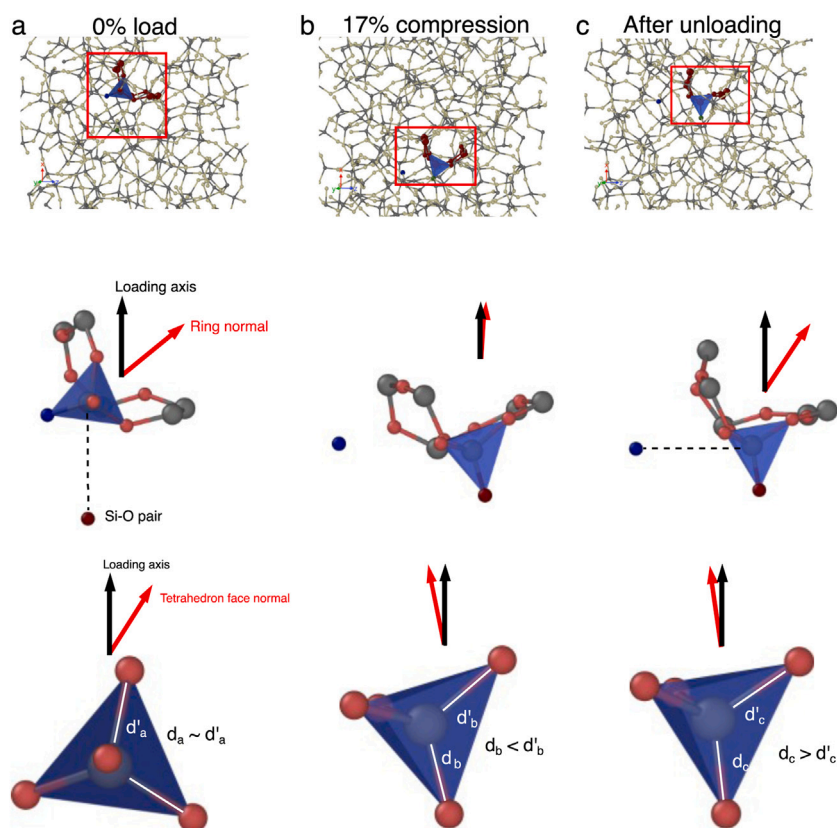


**Fig. 3.** Structural changes and mechanisms causing transient and persistent anisotropy during the MD simulation of uniaxial compression and unloading at RT. Always the same tetrahedron and ring are shown within a thin slice of the system. Changing positions are due to the homogeneous deformation. Details from configurations at (a) 0% strain, (b) at 17% compressive strain, and (c) after unloading from 17% compressive strain. First row: local detail of the silica glass network structure (gray: Si atoms, light yellow: O atoms), red Si and O atoms are used to highlight a 6-membered ring, a  $\text{SiO}_4$  tetrahedron from this ring is highlighted in blue, the green O atom is initially part of another tetrahedron. During compression to 17% strain, the central Si atom of the depicted tetrahedron changes its bonding topology by switching one bond to the green O atom. Second row: zoom in on the individual ring and tetrahedron, showing the reorientation of the ring normal, and highlighting the bond loss in the direction orthogonal to the compressive axis and the formation of a new bond along the loading axis, that does not change back to the original configuration. The entire process is shown in movie M1. Third row: zoom in on the tetrahedron, showing the change of the tetrahedra face normal orientation and comparing the lengths of Si–O bonds: in the unstrained configuration (a) all bonds have similar lengths; in (b) the newly formed bond parallel to the loading axis is shorter than bonds that are more orthogonal to the loading axis; in (c) this bond is longer than bonds orthogonal to the loading axis.

### 3.5. Anisotropy through high-temperature processing

In many industrial processes like fiber- or sheet-drawing, deformation takes place at temperatures above  $T_g$ . In order to mimic such experimental conditions, we have prepared anisotropic samples by applying the deformation at high-temperatures (HT), i.e., near  $T_g$ , similar to the procedure in Ref. [26], see the methods section for more details. The stress–strain curves, the transient and persistent anisotropy for different deformation temperatures are shown in Fig. S4 in the supplementary material. While the transient anisotropy is like the stress response systematically lower with increasing temperature, the magnitude of persistent anisotropy after quenching from 3000 K to 300 K and relaxing can – for tension – be similar to the one at 300 K. However, for compressive loading, the persistent anisotropy does not reach the same high values as for 300 and 600 K. The anisotropy of these samples as characterized by  $g_{20}(r)$  is shown in Fig. 4(a and b) together with the samples pre-deformed at RT. This plot clearly shows that the persistent anisotropy of glasses prepared through different routes has different structural origins; i.e., while the situation is more complex for the high-T deformed glasses than the RT deformed ones, the majority of short Si–O bonds are oriented after tensile predeformation at 3000 K orthogonal to the deformation axis, and parallel for compression. The situation is exactly the opposite for RT-predeformed glasses.

The measured transient anisotropy of these samples are significantly lower than for the glasses deformed at lower temperatures. This is attributed to the viscous nature of the high-temperature deformation

that involves much more bond breaking than during the mostly plastic deformation at RT, see Fig. S9 in the supplementary material. This prevents the formation of larger, anisotropic structures. This is also evident from Fig. S10 of the supplementary material, which shows in contrast to the situation at 300 K, at 3000 K no preferential orientation of Si–O bonds during loading is discernible. It is therefore not surprising that the quenched and relaxed samples have also a generally low value of the persistent anisotropy factor  $\alpha_p$ , see Fig. S4 in the supplementary material. However, for tensile deformation, the HT-quench method seems to yield slightly higher anisotropy than in compression and also than the tensile plastic deformation at RT, see Fig. S4 in the supplementary material. This method – akin to wire-drawing – thus yielded the highest persistent anisotropy in tension. This method of inducing anisotropy is expected to be even more interesting in glasses with partially-polymerized structures like in meta-silicate and meta-phosphate glasses as discussed in Section 3.3. The higher persistent anisotropy after compression at RT is due to the anomalous compressibility of pure silica glass, which allows for high plastic strains. Introducing anisotropy by compression is therefore best performed at RT.

## 4. Conclusion

Using novel structural analysis methods, we demonstrate that during MD simulations of uniaxial tension and compression at RT, the silica tetrahedra and the Si–O rings reorient themselves with respect

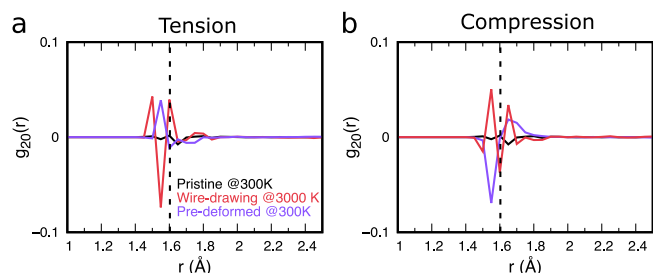


**Fig. 4.** Projection of the Si-O pair distribution function onto the spherical harmonic  $Y_{20}$  function comparing glasses with anisotropy induced through wire-drawing-like process at  $T_g$  and by mechanical pre-deformation at RT in tension (a) and compression (b). Black dashed lines indicate the average Si-O bond length in the pristine glass. Solid black: unstrained samples; purple: deformed to 17% strain and unloaded at RT, compare Fig. 1(c, d); red: pre-deformed to 17% strain at  $T_g$  and subsequently quenched and relaxed. See the discussion in the main text and of Fig. 1 for the interpretation of  $g_{20}(r)$ . (For interpretation of the references to color in this figure legend, the reader is referred to the web version of this article.)

to the loading axis, leading to transient anisotropy. During plastic deformation, only relatively few atoms change their bonding partners. The few bonds that broke during deformation were, however, preferentially oriented with respect to the loading axis: parallel for tension and orthogonal for compression. In contrast, the newly formed bonds were oriented orthogonal to the deformation axis for tension and parallel for compression. Few of these newly established bonds change during unloading, leading to persistent anisotropy in the stress-free glass. Persistent anisotropy is more pronounced after compression than after tension, as larger plastic strains can be reached in the former, while the glass shows limited plasticity and fractures under tension. Furthermore, it is shown that persistent anisotropy induced by mimicking a fiber-drawing process at  $T_g$  is structurally different from persistent anisotropy that results from deformation at RT.

The presented mechanistic insights into the emergence of different types of persistent anisotropy through different processing routes will enable new strategies for tailoring oxide glass properties and for designing new glasses for advanced technological applications.

#### Declaration of competing interest

The authors declare that they have no known competing financial interests or personal relationships that could have appeared to influence the work reported in this paper.

#### Acknowledgments

Financial support of this work was obtained from the German Science Foundation DFG through its priority program SPP 1594 "Topological Engineering of Ultra-strong Glasses". A.A, E.B and L.W. acknowledge funding from the European Research Council (ERC) under the European Union's Horizon 2020 research and innovation programme (grant agreement s No 725483 (A.A. and E.B.) and 681652 (L.W.)). J. G. acknowledge funding from the French ANR, grant ANR-21-CE08-0001. A.A thanks Dr.-Ing. Duancheng Ma for fruitful discussions. S.G. thanks Prof. Johannes Roth, Prof. James Kermode, Dr. Thomas Zeiser, and Dr. Faisal Shahzad for their help in the implementation and parallelization of silica force-fields in the IMD software package. The authors gratefully acknowledge the computer resources provided by the Erlangen Regional Computing Center (RRZE).

#### Appendix A. Supplementary data

Supplementary material related to this article can be found online at <https://doi.org/10.1016/j.actamat.2023.119108>.

#### References

- [1] G. Shakhgildyan, A. Lipatiev, S. Lotarev, S. Fedotov, V. Sigaev, Glass: Home of the periodic table, *Front. Chem.* 8 (2020) <http://dx.doi.org/10.3389/fchem.2020.00384>.
- [2] L. Wondraczek, E. Bouchbinder, A. Ehrlicher, J.C. Mauro, R. Sajzew, M.M. Smedskjaer, Advancing the mechanical performance of glasses: Perspectives and challenges, *Adv. Mater.* 34 (14) (2022) 2109029, <http://dx.doi.org/10.1002/adma.202109029>.
- [3] L. Wondraczek, J.C. Mauro, J. Eckert, U. Kühn, J. Horbach, J. Deubener, T. Rouxel, Towards ultrastrong glasses, *Adv. Mater.* 23 (39) (2011) 4578–4586, <http://dx.doi.org/10.1002/adma.201102795>.
- [4] R. Brückner, Properties and structure of vitreous silica. I, *J. Non-Crystalline Solids* 5 (2) (1970) 123–175, [http://dx.doi.org/10.1016/0022-3093\(70\)90190-0](http://dx.doi.org/10.1016/0022-3093(70)90190-0).
- [5] G.N. Greaves, S. Sen, Inorganic glasses, glass-forming liquids and amorphizing solids, *Adv. Phys.* 56 (1) (2007) 1–166, <http://dx.doi.org/10.1080/00018730601147426>.
- [6] B.P. Rodrigues, T. To, M.M. Smedskjaer, L. Wondraczek, Mechanical properties of oxide glasses, *Rev. Mineral. Geochem.* 87 (1) (2022) 229–281, <http://dx.doi.org/10.2138/rmg.2022.87.06>.
- [7] S. Inaba, H. Hosono, S. Ito, Entropic shrinkage of an oxide glass, *Nature Mater.* 14 (2014) 312, <http://dx.doi.org/10.1038/nmat4151>.
- [8] J. Endo, S. Inaba, S. Ito, Mechanical properties of anisotropic metaphosphate glass, *J. Am. Ceram. Soc.* 98 (9) (2015) 2767–2771, <http://dx.doi.org/10.1111/jace.13682>.
- [9] X. Yang, G. Scannell, C. Jain, B.P. Rodrigues, M.A. Schmidt, L. Wondraczek, Permanent structural anisotropy in a hybrid fiber optical waveguide, *Appl. Phys. Lett.* 111 (20) (2017) 201901, <http://dx.doi.org/10.1063/1.4999048>.
- [10] M.D. Lund, Y. Yue, Impact of drawing stress on the tensile strength of oxide glass fibers, *J. Am. Ceram. Soc.* 93 (10) (2010) 3236–3243, <http://dx.doi.org/10.1111/j.1551-2916.2010.03879.x>.
- [11] C.L. Rountree, D. Vandembroucq, M. Talamali, E. Bouchaud, S. Roux, Plasticity-induced structural anisotropy of silica glass, *Phys. Rev. Lett.* 102 (2009) 195501, <http://dx.doi.org/10.1103/PhysRevLett.102.195501>.
- [12] T. Sato, N. Funamori, T. Yagi, Differential strain and residual anisotropy in silica glass, *J. Appl. Phys.* 114 (10) (2013) 103509, <http://dx.doi.org/10.1063/1.4820263>.
- [13] M. Ya, J. Deubener, Y. Yue, Enthalpy and anisotropy relaxation of glass fibers, *J. Am. Ceram. Soc.* 91 (3) (2008) 745–752, <http://dx.doi.org/10.1111/j.1551-2916.2007.02100.x>.
- [14] M. Ballauff, J.M. Brader, S.U. Egelhaaf, M. Fuchs, J. Horbach, N. Koumakis, M. Krüger, M. Laurati, K.J. Mutch, G. Petekidis, M. Siebenbürger, T. Voigtmann, J. Zausch, Residual stresses in glasses, *Phys. Rev. Lett.* 110 (21) (2013) 215701, <http://dx.doi.org/10.1103/PhysRevLett.110.215701>.
- [15] Z. Pan, O. Benzine, S. Sawamura, R. Limbach, A. Koike, T.D. Bennett, G. Wilde, W. Schirmacher, L. Wondraczek, Disorder classification of the vibrational spectra of modern glasses, *Phys. Rev. B* 104 (13) (2021) <http://dx.doi.org/10.1103/physrevb.104.134106>.
- [16] O. Benzine, S. Bruns, Z. Pan, K. Durst, L. Wondraczek, Local deformation of glasses is mediated by rigidity fluctuation on nanometer scale, *Adv. Sci.* 5 (10) (2018) 1800916, <http://dx.doi.org/10.1002/advs.201800916>.
- [17] S.K. Lee, P.J. Eng, H. Kwang Mao, Y. Meng, M. Newville, M.Y. Hu, J. Shu, Probing of bonding changes in B2O3 glasses at high pressure with inelastic X-ray scattering, *Nature Mater.* 4 (11) (2005) 851–854, <http://dx.doi.org/10.1038/nmat1511>.
- [18] R. Brueckner, Anisotropic glasses and glass melts : a survey, *Glass Sci. Technol.* 69 (1996) 396–411.
- [19] L.N.G. Filon, F. Harris, On the di-phasic nature of glass, as shown by photo-elastic observations, *Proc. R. Soc. Lond. Series A Contain. Pap. A Math. Phys. Character* 103 (723) (1923) 561–571, <http://dx.doi.org/10.1098/rspa.1923.0078>.
- [20] T. Takamori, M. Tomozawa, Anomalous birefringence in oxide glasses, in: *Glass I: Interaction with Electromagnetic Radiation - Treatise on Materials Science and Technology*, Elsevier, 1977, pp. 123–155, [http://dx.doi.org/10.1016/s0161-9160\(13\)70053-x](http://dx.doi.org/10.1016/s0161-9160(13)70053-x).
- [21] Y. Suzuki, J. Haimovich, T. Egami, Bond-orientational anisotropy in metallic glasses observed by x-ray diffraction, *Phys. Rev. B* 35 (5) (1987) 2162–2168, <http://dx.doi.org/10.1103/physrevb.35.2162>.
- [22] B. Champagnon, S. Degioanni, C. Martinet, Anisotropic elastic deformation of silica glass under uniaxial stress, *J. Appl. Phys.* 116 (12) (2014) 123509, <http://dx.doi.org/10.1063/1.4896401>.
- [23] M. Maković, F. Niekkel, L. Wondraczek, E. Bitzek, E. Spiecker, In situ mechanical quenching of nanoscale silica spheres in the transmission electron microscope, *Scr. Mater.* 121 (2016) 70–74, <http://dx.doi.org/10.1016/j.scriptamat.2016.04.019>.
- [24] J. Du, Molecular dynamics simulations of oxide glasses, in: *Springer Handbook of Glass*, Springer International Publishing, 2019, pp. 1131–1155, [http://dx.doi.org/10.1007/978-3-319-93728-1\\_32](http://dx.doi.org/10.1007/978-3-319-93728-1_32).
- [25] S. Ghemid, A. Monteil, D. Guichaoua, Orientation of silica rings under uniaxial stress in simulated vitreous silica, *Comput. Mater. Sci.* 39 (3) (2007) 552–556, <http://dx.doi.org/10.1016/j.commatsci.2006.08.006>.

- [26] X. Bidault, S. Chaussedent, W. Blanc, D.R. Neuville, Deformation of silica glass studied by molecular dynamics: Structural origin of the anisotropy and non-Newtonian behavior, *J. Non-Crystalline Solids* 433 (2016) 38–44, <http://dx.doi.org/10.1016/j.jnoncrysol.2015.11.029>.
- [27] J.R. Kermode, S. Cereda, P. Tangney, A. De Vita, A first principles based polarizable O(N) interatomic force field for bulk silica, *J. Chem. Phys.* 133 (9) (2010) 094102, <http://dx.doi.org/10.1063/1.3475565>.
- [28] B.W.H. van Beest, G.J. Kramer, R.A. van Santen, Force fields for silicas and aluminophosphates based on ab initio calculations, *Phys. Rev. Lett.* 64 (16) (1990) 1955–1958, <http://dx.doi.org/10.1103/physrevlett.64.1955>.
- [29] C. Rajappa, S.B. Sringeri, Y. Subramanian, J. Gopalakrishnan, A molecular dynamics study of ambient and high pressure phases of silica: Structure and enthalpy variation with molar volume, *J. Chem. Phys.* 140 (24) (2014) 244512, <http://dx.doi.org/10.1063/1.4885141>.
- [30] R.L. Mozzi, B.E. Warren, The structure of vitreous silica, *J. Appl. Crystallogr.* 2 (4) (1969) 164–172, <http://dx.doi.org/10.1107/S0021889869006868>.
- [31] W.G. Hoover, Canonical dynamics: Equilibrium phase-space distributions, *Phys. Rev. A* 31 (3) (1985) 1695–1697, <http://dx.doi.org/10.1103/physreva.31.1695>.
- [32] M. Parrinello, A. Rahman, Polymorphic transitions in single crystals: A new molecular dynamics method, *J. Appl. Phys.* 52 (12) (1981) 7182–7190, <http://dx.doi.org/10.1063/1.328693>.
- [33] S.L. Roux, P. Jund, Ring statistics analysis of topological networks: New approach and application to amorphous GeS<sub>2</sub> and SiO<sub>2</sub> systems, *Comput. Mater. Sci.* 49 (1) (2010) 70–83, <http://dx.doi.org/10.1016/j.commatsci.2010.04.023>.
- [34] J. Luo, J. Wang, E. Bitzek, J.Y. Huang, H. Zheng, L. Tong, Q. Yang, J. Li, S.X. Mao, Size-dependent brittle-to-ductile transition in silica glass nanofibers, *Nano Lett.* 16 (1) (2016) 105–113, <http://dx.doi.org/10.1021/acs.nanolett.5b03070>, PMID: 26569137.
- [35] S. Hess, *Tensors for physics*, Springer, 2015.
- [36] N.M. Trease, T.M. Clark, P.J. Grandinetti, J.F. Stebbins, S. Sen, Bond length-bond angle correlation in densified silica—Results from 17 O NMR spectroscopy, *J. Chem. Phys.* 146 (18) (2017) <http://dx.doi.org/10.1063/1.4983041>.
- [37] C. Benmore, E. Soignard, S. Amin, M. Guthrie, S. Shastri, P. Lee, J. Yarger, Structural and topological changes in silica glass at pressure, *Phys. Rev. B* 81 (5) (2010) 054105, <http://dx.doi.org/10.1103/PhysRevB.81.054105>.
- [38] H. He, S.H. Hahn, J. Yu, Q. Qiao, A.C. van Duin, S.H. Kim, Friction-induced subsurface densification of glass at contact stress far below indentation damage threshold, *Acta Mater.* 189 (2020) 166–173, <http://dx.doi.org/10.1016/j.actamat.2020.03.005>.
- [39] H. He, Z. Chen, Y.T. Lin, S.H. Hahn, J. Yu, A.C. van Duin, T.D. Gokus, S.V. Rotkin, S.H. Kim, Subsurface structural change of silica upon nanoscale physical contact: Chemical plasticity beyond topographic elasticity, *Acta Mater.* 208 (2021) <http://dx.doi.org/10.1016/j.actamat.2021.116694>.